

# High-pressure phase of brucite stable at Earth's mantle transition zone and lower mantle conditions

Andreas Hermann<sup>a,b,1</sup> and Mainak Mookherjee<sup>c</sup>

<sup>a</sup>School of Physics and Astronomy, The University of Edinburgh, Edinburgh EH9 3FD, United Kingdom; <sup>b</sup>Centre for Science at Extreme Conditions, The University of Edinburgh, Edinburgh EH9 3FD, United Kingdom; and <sup>c</sup>Earth Materials Laboratory, Earth, Ocean and Atmospheric Sciences, Florida State University, Tallahassee, FL 32310

Edited by Roald Hoffmann, Cornell University, Ithaca, NY, and approved October 26, 2016 (received for review July 14, 2016)

**We investigate the high-pressure phase diagram of the hydrous mineral brucite,  $\text{Mg}(\text{OH})_2$ , using structure search algorithms and ab initio simulations. We predict a high-pressure phase stable at pressure and temperature conditions found in cold subducting slabs in Earth's mantle transition zone and lower mantle. This prediction implies that brucite can play a much more important role in water transport and storage in Earth's interior than hitherto thought. The predicted high-pressure phase, stable in calculations between 20 and 35 GPa and up to 800 K, features  $\text{MgO}_6$  octahedral units arranged in the anatase- $\text{TiO}_2$  structure. Our findings suggest that brucite will transform from a layered to a compact 3D network structure before eventual decomposition into periclase and ice. We show that the high-pressure phase has unique spectroscopic fingerprints that should allow for straightforward detection in experiments. The phase also has distinct elastic properties that might make its direct detection in the deep Earth possible with geophysical methods.**

brucite | pressure | phase transition | electronic structure calculations

**W**ater plays an important role in sustaining geological activity. For instance, water helps in lowering the mantle's melting temperature, enhancing diffusion and creep thus affecting rheology of rocks, and also influences mineral phase boundaries. Current estimates suggest that the Earth's mantle is likely to contain a mass of water equivalent to the mass of the world's oceans (1, 2). The exchange of water between the surface and deep mantle reservoirs is vital for the sustenance of surface water over geological time scales (3). Hydrous minerals stable in the hydrated oceanic crust and mantle play an important role in transporting water into the Earth's interior. Hydrated peridotite, the major mantle rock type, can be understood by considering mineral phases stable in the ternary system of  $\text{MgO}$ - $\text{SiO}_2$ - $\text{H}_2\text{O}$  (MSH). Brucite,  $\text{Mg}(\text{OH})_2$ , is arguably the simplest hydrous mineral in the MSH system. Brucite is also the most important  $\text{MgO}$ - $\text{H}_2\text{O}$  binary and the most water-rich phase within the MSH ternary system.

The crystal structure of brucite consists of  $\text{Mg}^{2+}$  cations and  $\text{OH}^-$  anions arranged in layers, in an overall trigonal structure (space group symmetry  $P3m1$ ); Fig. 1. The common ionic compound  $\text{CdI}_2$  is the archetype crystal structure for brucite as well as for portlandite [ $\text{Ca}(\text{OH})_2$ ] and several other transition metal hydroxides  $\text{M}(\text{OH})_2$  where  $\text{M} = \text{Mn}, \text{Ni}, \text{Co}, \text{Fe}, \text{Cd}$ , etc. (4–10). In brucite, the crystal structure comprises layers of edge-sharing  $\text{MgO}_6$  polyhedra. The interaction between the layers is weak at ambient conditions, where each upward-pointing OH group is surrounded by three downward-pointing OH groups in the adjacent layer and vice versa. Under compression the H–H repulsive interactions lead to positional disordering of the protons, which are displaced from the  $2d$  Wyckoff site into one of three equivalent  $6i$  sites as documented from neutron diffraction studies (11, 12). Vibrational spectroscopic studies including infrared and Raman spectroscopy show a broad  $\nu_{\text{OH}}$  stretching band with the appearance of additional bands upon compression. The appearance of additional bands hints at the pressure-induced frustrations of the proton (13, 14). First-principles molecular dynamics simulations

also demonstrated the proton frustrations in brucite and portlandite at high pressure (15). A first-principles study at static conditions indicated that the pressure-induced hydrogen bonding in brucite is weak or unlikely to occur within the thermodynamic stability field of brucite (16). In addition, the study also predicted that upon compression, protons may transition from a dynamic positional disorder to a static positional disorder, leading to a lowering of the trigonal symmetry to  $P3$ .

Layered structures similar to that of brucite are also common in group I (alkali) hydroxides. Under pressure, the alkali hydroxides tend not only to form hydrogen bonds between the layers, but undergo transitions to 3D network structures, with 0-, 1-, or 2-dimensional hydrogen-bonded sublattices (17–20). The rationale from the high-pressure behavior of those systems is that layered phases are ultimately too loosely packed to survive under pressure. The important question relevant for deep Earth geophysics is whether brucite will undergo a similar transition and densification at high pressures, and significantly deviate from a layered structure, before decomposition into  $\text{MgO}$  and  $\text{H}_2\text{O}$  occurs. The presence of such a phase would have a significant impact on whether brucite itself could be stable in the mantle transition zone and lower mantle (potentially with quite different properties than those of the known phase), as well as the relative stability of competing MSH phases. We address this question here using structure prediction methods and first-principles total energy calculations, which enable us to bypass potential difficulties in high-pressure experiments such as sample preparation or kinetic reaction barriers. In recent years, such calculations have been crucial in making important predictions of high-pressure phases relevant for solid Earth geophysics (21, 22). These have been very helpful for experimental discoveries (23). Here, we suggest that brucite transforms to a new high-pressure

## Significance

**Hydrous minerals help transport water deep into Earth's mantle, and form part of a cycle that regulates the sustained presence of surface water on Earth. To understand the deep-water cycle, it is crucial to study the properties of hydrous minerals under the conditions present in Earth's mantle. Brucite is one of the simplest hydrous minerals and stores significant amounts of water as hydroxyl groups. It is assumed to decompose in the mantle transition zone, but we show here that a more compact high-pressure phase is stabilized instead that pushes the stability region of brucite into the lower mantle. Brucite might be present in much larger quantities, and play a larger role in water transport and storage, than previously thought.**

Author contributions: A.H. designed research; A.H. and M.M. performed research; A.H. and M.M. analyzed data; and A.H. and M.M. wrote the paper.

The authors declare no conflict of interest.

This article is a PNAS Direct Submission.

Data deposition: Supplementary research data, in compliance with Engineering and Physical Sciences Research Council (EPSRC) research data policy, can be accessed at [dx.doi.org/10.7488/ds/1519](https://dx.doi.org/10.7488/ds/1519).

<sup>1</sup>To whom correspondence should be addressed. Email: [a.hermann@ed.ac.uk](mailto:a.hermann@ed.ac.uk).

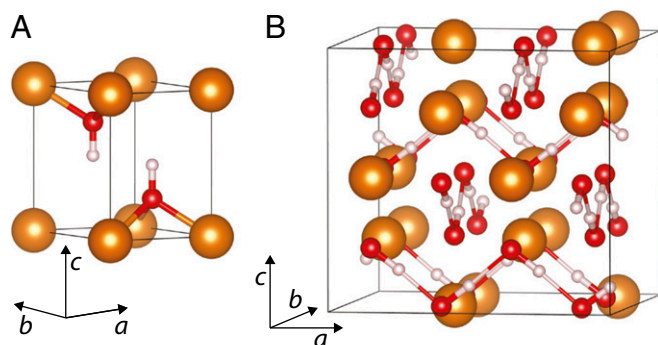


**Fig. 1.** (A) Low-pressure phase of brucite with  $P\bar{3}m1$  space group symmetry. (B) High-pressure phase of  $Mg(OH)_2$  with tetragonal  $P4_12_12$  space group symmetry. Both the structures are drawn to the same scale at  $P = 20$  GPa. Gold (red, white) spheres denote Mg (O, H) atoms. Hydrogen bonds in the tetragonal phase are indicated by thin lines.

phase at conditions relevant to subducting slabs in the mantle transition zone and lower mantle, i.e., pressures of  $\sim 20$  GPa and temperatures of  $\sim 800$  K.

## Results

Our density-functional calculations give excellent agreement for the structural parameters of brucite ( $P\bar{3}m1$ ) with experimental data at  $P = 1$  atm (Table 1). They also correctly reproduce the pressure-induced stabilization of hydrogen bond formation and static proton disorder, in the form of the  $P\bar{3}$  phase (16) (Fig. 2, *Upper*). For those two known brucite phases, decomposition into periclase (MgO) and ice-VIII is then calculated to occur at 18 and 21 GPa, respectively, i.e., in the Earth mantle transition zone. This agrees reasonably well with thermodynamic modeling based on the measured  $P$ - $V$ - $T$  equation of state for brucite, which estimated a decomposition pressure of 27 GPa at  $T = 300$  K (24). Note that brucite has been compressed significantly beyond this pressure, likely due to kinetic barriers in the decomposition reaction (24, 25).

Our crystal structure prediction runs, however, revealed a candidate for a high-pressure phase of  $Mg(OH)_2$  with tetragonal space group symmetry ( $P4_12_12$ ), which is energetically more stable than both known modifications above 17 GPa (Fig. 2, *Upper*). With the appearance of a high-pressure phase, the thermodynamic stability limit of  $Mg(OH)_2$  (toward decomposition into MgO and ice) is shifted to significantly higher pressures: by 8 GPa in the ground state, from 21 to 29 GPa. This delays the decomposition of  $Mg(OH)_2$  from the lower part of the mantle transition zone (the pressure region 13–21 GPa) (26) deep into the lower mantle. The stability of the tetragonal  $Mg(OH)_2$  phase is unaffected by the choice of exchange-correlation functional or the inclusion of zero-point effects (ZPEs). For instance, using the van der Waals density-functional approach (vdW-DF) with the optB88 functional (27–30), which includes dispersion interactions based on the electronic density, instead of the semilocal Perdew–Burke–Ernzerhof (PBE) functional, we find tetragonal  $Mg(OH)_2$  to be stable from 18 to 27 GPa. When ZPEs are included with the PBE functional, tetragonal  $Mg(OH)_2$  is stable from 19 to 33 GPa.

We used the quasi-harmonic approximation to estimate the Gibbs free energies of the relevant phases and construct the finite-temperature phase diagram of  $Mg(OH)_2$ . To that end, we included the vibrational contribution to the entropy of each phase, which results in

$$F(T, V) = E_0(V) + k_B T \int_0^\infty g(\omega) \ln \left[ 2 \sinh \left( \frac{\hbar \omega}{2k_B T} \right) \right] d\omega,$$

where  $g(\omega)$  is the phonon density of states obtained from finite displacement calculations. As shown in Fig. 2 (*Lower*), this results in a large stability field for the tetragonal  $Mg(OH)_2$  phase, up to  $T = 800$  K at 30 GPa, where it forms a triple point with brucite (in the  $P\bar{3}$  model) and the decomposition into MgO + ice-VIII. This triple point corresponds to a depth of  $\sim 800$  km, in the upper reaches of the lower mantle, and approaches cold geothermal gradients estimated for subducting slabs (23, 31, 32) and the melting line of ice (33, 34). We included in this phase diagram the calculated geotherm for old and rapidly descending slabs as a solid blue line (32). This should serve as a low-temperature

**Table 1.** Crystallographic data of  $Mg(OH)_2$  phases

Phase	Pressure	Lattice constants	Atomic positions
$P\bar{3}m1$ (Exp)	1 atm	$a = b = 3.150$ Å, $c = 4.770$ Å $\alpha = \beta = 90^\circ, \gamma = 120^\circ$	Mg(0,0,0) O(1/3, 2/3, 0.220) H(1/3, 2/3, 0.413)
$P\bar{3}m1$ (DFT)	1 atm	$a = b = 3.182$ Å, $c = 4.801$ Å $\alpha = \beta = 90^\circ, \gamma = 120^\circ$	Mg(0, 0, 0) O(1/3, 2/3, 0.217) H(1/3, 2/3, 0.419)
$P\bar{3}$	10 GPa	$a = b = 5.310$ Å, $c = 4.383$ Å $\alpha = \beta = 90^\circ, \gamma = 120^\circ$	Mg1(0, 0, 0) Mg2(1/3, 2/3, -0.018) O(-0.006, -0.336, -0.239) H(-0.070, -0.365, -0.451)
$P4_12_12$	20 GPa	$a = b = 8.178$ Å, $c = 7.549$ Å $\alpha = \beta = \gamma = 90^\circ$	Mg1(0.380, 0.380, 0) Mg2(-0.130, -0.130, 0) Mg3(-0.370, 0.120, 0.5) O1(-0.120, 0.372, 0.266) O2(0.370, -0.122, 0.266) O3(-0.122, 0.120, 0.016) O4(0.372, -0.370, 0.016) H1(-0.126, -0.477, 0.404) H2(0.381, 0.227, 0.404) H3(0.227, 0.129, 0.154) H4(-0.477, -0.378, 0.154)

Optimized crystal structures of various brucite phases, from ground-state DFT-PBE calculations. First row gives experimental results for the  $P\bar{3}m1$  phase at  $P = 1$  atm from powder neutron diffraction (12).

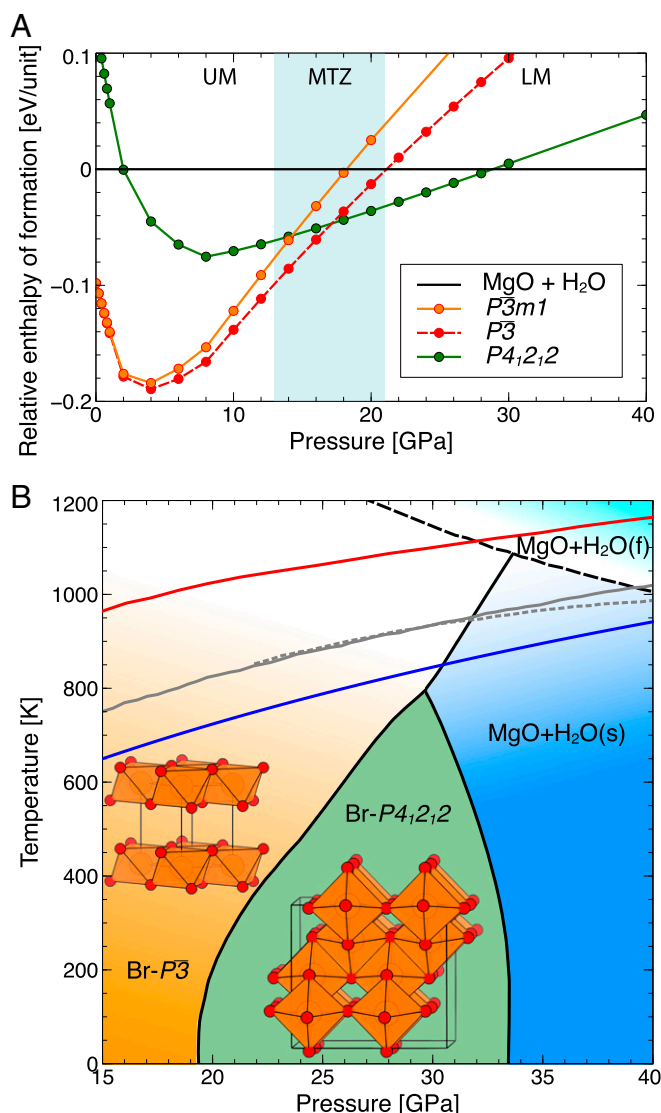


**Fig. 2.** Thermodynamic phase diagram of  $\text{Mg}(\text{OH})_2$ . (A) Ground-state enthalpies of formation of various  $\text{Mg}(\text{OH})_2$  phases, relative to decomposition into  $\text{MgO}$  and ice-VIII. The light-blue band represents the pressures relevant for the mantle transition zone (MTZ), upper- (UM) and lower (LM) mantle. (B) Computationally derived thermodynamic phase diagram for  $\text{Mg}(\text{OH})_2$ . Also shown are a parameterized high-temperature decomposition curve (dashed black line) (24), cold and typical slab geotherms (blue and red solid lines) (23, 32), and ice melting lines (solid and dotted gray lines) (33, 34).

boundary for mantle slab geotherms (we extrapolated the data from ref. 32 beyond 20 GPa in a power expansion). We did not consider nuclear quantum effects in the construction of the phase diagram. Those can play an important role in aqueous systems (35) and might affect the phase transition pressures in the low-temperature region in particular if the protons' chemical environment differs significantly across the respective phases. There is some indication (see below) that the hydrogen bonds in tetragonal  $\text{Mg}(\text{OH})_2$  are stronger than in brucite.

The tetragonal  $\text{Mg}(\text{OH})_2$  phase ( $P4_12_12_1$ ) is very different from the low-pressure layered phase (Fig. 1; see Table 1 for structural data). The high-pressure phase forms a 3D network of edge-sharing  $\text{MgO}_6$  octahedral units. In fact, the phase (when ignoring protons) is isostructural with the anatase- $\text{TiO}_2$  crystal structure, but with  $\text{MgO}_6$  octahedral units that are less distorted compared with the  $\text{TiO}_6$  octahedral units in anatase (Fig. 2, *Lower, Inset*).

The protons are located in channels in between the  $\text{MgO}_6$  polyhedral units. Alternatively, the crystal structure can be characterized by zigzag hydrogen-bonded  $\text{O-H}\cdots\text{O-H}$  chains running along the  $a$  and  $b$  directions, and which are lying in the  $bc$  and  $ac$  planes, respectively. In the ground state, the  $\text{O-H}$  vectors order antiferroelectrically (Fig. 1), but it is very likely that proton disorder sets in at finite temperatures. The major structural differences compared with the low-pressure phase of brucite suggest that there are significant kinetic barriers to transform from the layered phase into the tetragonal phase (just as for the decomposition), which would explain why the transition has not been observed in room-temperature experiments to pressures well into the predicted pressure stability region of the tetragonal phase.

The pressure–volume relation for brucite ( $P\bar{3}$ ) can be described by a Birch–Murnaghan equation of state with equilibrium volume  $V_0^{P\bar{3}} = 41.68 (\pm 0.09) \text{ \AA}^3$ , bulk modulus  $K_0^{P\bar{3}} = 43.4 (\pm 1.1) \text{ GPa}$ , and its pressure derivative  $K_0'^{P\bar{3}} = 5.39 (\pm 0.10)$ . In contrast to brucite, the 3D network of  $\text{MgO}_6$  polyhedra in tetragonal  $\text{Mg}(\text{OH})_2$  allows for a substantially more compact packing with  $V_0^{P4_12_12} = 38.06 (\pm 0.07) \text{ \AA}^3$ ,  $K_0^{P4_12_12} = 67.3 (\pm 1.6) \text{ GPa}$ , and  $K_0'^{P4_12_12} = 4.91 (\pm 0.09)$ . At 1 bar the tetragonal phase is 8.67% smaller than brucite, and stiffer by ~55%. At 20 GPa, where tetragonal  $\text{Mg}(\text{OH})_2$  has the lower enthalpy, it is 3.8% more compact than the brucite ( $P\bar{3}$ ) phase.

Although the tetragonal phase is denser compared with the brucite phase, at 1 bar the full elastic stiffness tensor reveals significant anisotropy. The principal stiffness components are related as  $c_{11}^{P4_12_12} \sim 1.5 \times c_{33}^{P4_12_12}$ ,  $c_{12}^{P4_12_12} \geq c_{13}^{P4_12_12}$ , and the shear stiffness components are related as  $c_{44}^{P4_12_12} \geq c_{66}^{P4_12_12}$  (Fig. 3). At zero pressure (i.e., 1 bar), the Hill-averaged bulk ( $K_{Hill}^{P4_12_12}$ ) and shear ( $G_{Hill}^{P4_12_12}$ ) moduli are 69.5 and 55.4 GPa, respectively, for the tetragonal  $\text{Mg}(\text{OH})_2$  phase. This is significantly stiffer than the bulk ( $K_{Hill}^{P3}$ ) and shear ( $G_{Hill}^{P3}$ ) moduli for the trigonal phase, 46.7 and 36.4 GPa, respectively (36). The compressional ( $V_P$ ) and shear ( $V_S$ ) sound velocities for the tetragonal phase are also faster compared with the trigonal phase (Fig. 3).

In addition to changes in the velocities, brucite and tetragonal  $\text{Mg}(\text{OH})_2$  have quite distinct elastic anisotropy. At low pressures ( $\sim 0$  GPa), the brucite phase has significant  $V_P$ - and  $V_S$ -elastic anisotropy, 57 and 46%, respectively. In comparison, tetragonal  $\text{Mg}(\text{OH})_2$  has modest  $V_P$ - and  $V_S$ -elastic anisotropies of 20% and 13%, respectively (Fig. 4). At higher pressures, as the layered nature of the compound becomes less pronounced, the elastic anisotropy in brucite reduces, with the  $V_P$  elastic anisotropy decreasing at a faster rate than the  $V_S$  anisotropy. In other words, the pressure derivative of  $C_{33}$  is greater than the pressure derivative of  $C_{11}$ , i.e.,  $dC_{11}/dP < dC_{33}/dP$ . For tetragonal  $\text{Mg}(\text{OH})_2$  at higher pressure, the  $V_P$  elastic anisotropy reduces and remains fairly constant over the pressure range that corresponds to the entire upper mantle, transition zone, and lower mantle. The S-wave elastic anisotropy for tetragonal  $\text{Mg}(\text{OH})_2$ , on the other hand, increases almost linearly upon compression beyond 5 GPa. In this phase, the pressure derivative of  $C_{11}$  is slightly greater than the pressure derivative of  $C_{33}$ , i.e.,  $dC_{11}/dP > dC_{33}/dP$ . In addition, even though the octahedral network in the tetragonal phase is 3D, hydrogen bonds that additionally constrain the elastic response are essentially confined along the  $a$  and  $b$  directions. The predicted anisotropies could provide another diagnostic test for the presence of tetragonal  $\text{Mg}(\text{OH})_2$  in the deep mantle, but need to be accompanied by an understanding of the rheological parameters including the slip systems, the combined elastic anisotropy and lattice preferred orientation to relate these calculated numbers to the seismic anisotropy observed in the deep mantle and in subduction zone settings.

Tetragonal  $\text{Mg}(\text{OH})_2$  is an ionic compound. A topological analysis of the electron density based on Bader's quantum theory of atoms in molecules (37) suggests partial atomic charges of +1.61/−0.80 electrons for  $\text{Mg}^{2+}$  and  $\text{OH}^-$  ions, respectively, at 20 GPa. This is very similar to the partial charges of +1.65/−0.82 electrons in



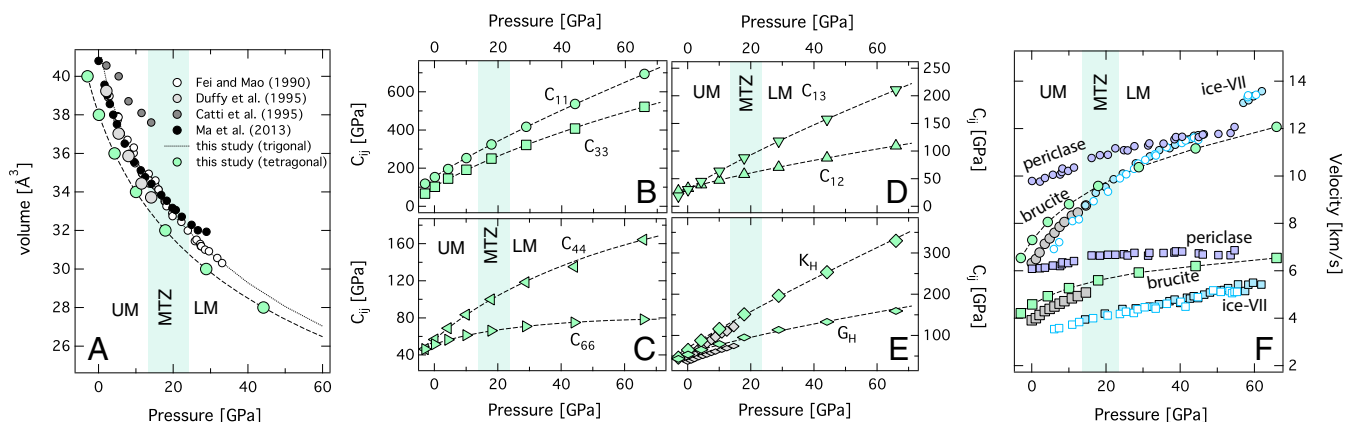


**Fig. 3.** Equation of state, elasticity, and sound velocity of  $\text{Mg}(\text{OH})_2$ . (A) Plot of volume as a function of pressure. Green symbols and thin dotted line refer to the  $P4_12_12$ - and  $P3$ - $\text{Mg}(\text{OH})_2$  phases, respectively. The dashed line gives the finite strain fit to the  $P4_12_12$  phase. Experimental results are shown in filled light gray (single-crystal X-ray diffraction); dark gray (powder neutron diffraction); black and white symbols (synchrotron-based powder X-ray diffraction), from refs. 12, 14, 24, 25. (B–D) The full elastic stiffness tensor components, and (E) Hill-averaged bulk ( $K_H$ ) and shear ( $G_H$ ) moduli for tetragonal  $\text{Mg}(\text{OH})_2$  as function of pressure. (F) Calculated compressional/shear sound-wave velocities (circles/squares) for tetragonal  $\text{Mg}(\text{OH})_2$  (light-green symbol). Gray symbols refer to the experimentally determined sound velocity of brucite (36). Experimental data are given for the decomposition products periclase ( $\text{MgO}$ ) (filled blue symbols) (63) and ice-VII (filled light-blue symbols: compression; white symbols: decompression) (50).

brucite ( $P3$ ) at the same pressure. The high-pressure phase does, however, feature stronger hydrogen bonds, as the structural rearrangement in  $P4_12_12$  results in much shorter hydrogen-bonded separations: at 20 GPa,  $d_{\text{O}\cdots\text{O}} = 1.62 \text{ \AA}$ , compared with  $1.87 \text{ \AA}$  in the  $P3$  phase. As a consequence, the covalent O–H bonds are somewhat extended and arguably weakened in the  $P4_12_12$  phase. At 20 GPa, the hydroxyl bond length  $d_{\text{OH}}$  is  $\sim 1.01 \text{ \AA}$  for  $P4_12_12$  compared with  $0.98 \text{ \AA}$  in the  $P3$  phase.

The changes in the hydrogen bonding lead to significant differences in the vibrational properties, which should make detection of the high-pressure phase quite straightforward. In Fig. 5, we show calculated O–H stretch modes of the different phases as a function of  $d_{\text{O}\cdots\text{O}}$  distance, compared with an empirical functional relation established from experimental spectroscopic data on hydrous minerals (38). Calculated frequencies for the  $P3m1$  and  $P3$  phases, as has been noted before (39, 40), give good

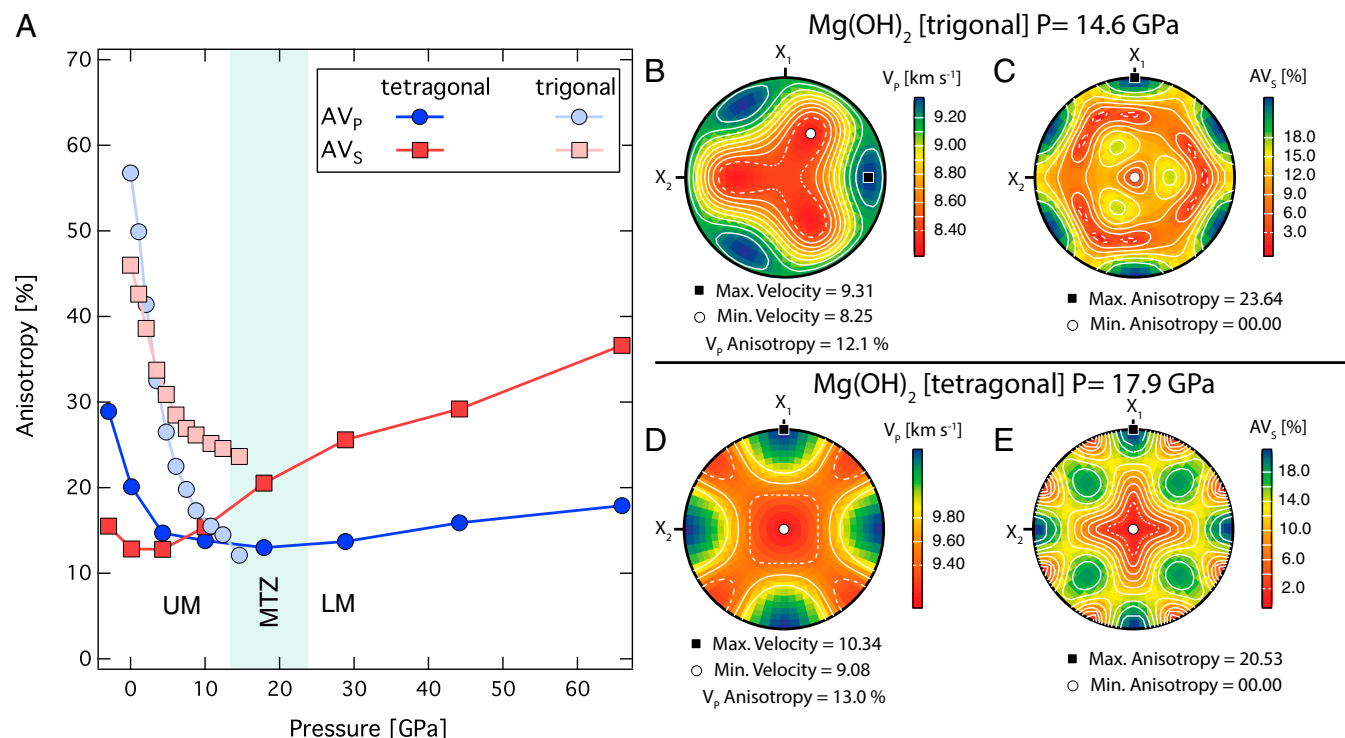


**Fig. 4.** Elastic anisotropy of  $\text{Mg}(\text{OH})_2$ . (A) Plot of P-wave anisotropy ( $AV_p$ , blue) and S-wave anisotropy ( $AV_s$ , red) as a function of pressure. The light and dark color symbols correspond to trigonal (brucite) and tetragonal  $\text{Mg}(\text{OH})_2$ , respectively. (B and D) show the stereographic projection of the P-wave velocity variations across the orthogonal directions for both phases. (C and E) show the stereographic projection of the S-wave anisotropy variations across the orthogonal directions for both phases. The orthogonal coordinates  $X_1$  and  $X_2$  are shown in the stereographic projections. The  $X_3$  axis is perpendicular to both  $X_1$  and  $X_2$  axes. The color shadings are in inverse logarithmic scales. The minimum and maximum velocity directions for tetragonal  $\text{Mg}(\text{OH})_2$  along the  $X_3$  and  $X_1$  axes coincide with the extremal  $C_{33}$  and  $C_{11}$  elastic constants, respectively.



the Vienna Ab initio Simulation Package (53–55). Plane-wave cutoffs of  $E_c = 800$  eV and k-point sampling densities of  $20/\text{\AA}^{-1}$  were found to give sufficiently converged energies and forces. Electronic exchange–correlation energies are approximated with the PBE generalized gradient functional (56), and geometries were optimized until remaining forces on the atoms were smaller than  $1 \text{ meV/\AA}$ .

Crystal structure predictions were then run at 20, 50, and 100 GPa, with two and four formula units per unit cell, and using approaches based on evolutionary algorithms and the particle swarm optimization method as implemented in the XtalOpt and CALYPSO packages (57, 58). Around 600 structures were optimized in each search run. Phonon dispersions and densities of state were obtained with the finite displacement method using the PHON program and appropriate supercells of the relevant structures, with central difference displacements of  $\pm 0.02 \text{ \AA}$  and up to 640 atoms (59).

We applied  $\pm 1\%$  strains to accurately determine the stresses in the limit of small strain (60). The elastic constants  $c_{ij}$  were obtained from the stress–strain relation,

$\sigma_i = c_{ij} \epsilon_j$  (in Voigt notation) (61). The pressure dependence of the full elastic stiffness tensor was fitted with the finite strain formulation (60). The P-wave and S-wave anisotropy are defined as  $AV_p = 100 \times (V_{p\max} - V_{p\min}) / ((V_{p\max} + V_{p\min}) / 2)$  and  $AV_s = 100 \times (V_{s\max} - V_{s\min}) / ((V_{s\max} + V_{s\min}) / 2)$ , respectively. We used petrophysical software to determine the elastic anisotropy (62).

**ACKNOWLEDGMENTS.** The authors thank David Mainprice for sharing elasticity data on trigonal brucite. A.H. thanks John S. Loveday for fruitful discussions. M.M. is supported by National Science Foundation Grant EAR/1639552 and the Council of Research and Creativity, Florida State University. Computational resources provided by the UK National Supercomputing Service through the UK Car–Parrinello (UKCP) consortium [funded by Engineering and Physical Sciences Research Council (EPSRC) Grant EP/K01465X] and Project ID d56 “Planetary Interiors,” by the Condensed Matter Centre for Doctoral Training (funded by EPSRC Grant EP/L015110/1), and by the Royal Society (Research Grant RG150247) are gratefully acknowledged.

- Pearson DG, et al. (2014) Hydrous mantle transition zone indicated by ringwoodite included within diamond. *Nature* 507(7491):221–224.
- Schmandt B, Jacobsen SD, Becker TW, Liu Z, Dueker KG (2014) Earth's interior. Dehydration melting at the top of the lower mantle. *Science* 344(6189):1265–1268.
- Hirschmann MM (2006) Water, melting, and the deep earth  $\text{H}_2\text{O}$  cycle. *Annu Rev Earth Planet Sci* 34:629–653.
- Pavese A, Catti M, Ferraris G, Hull S (1997) P–V equation of state of portlandite,  $\text{Ca}(\text{OH})_2$ , from powder neutron diffraction data. *Phys Chem Miner* 24:85–89.
- Parise JB, et al. (1998) Pressure dependence of hydrogen bonding in metal deuteriooxides: A neutron powder diffraction study of  $\text{Mn}(\text{OD})_2$  and  $\beta\text{-Co}(\text{OD})_2$ . *Phys Chem Miner* 25:130–137.
- Parise JB, Loveday JS, Nelmis RJ, Kagi H (1999) Hydrogen repulsion “transition” in  $\text{Co}(\text{OD})_2$  at high pressure? *Phys Rev Lett* 83:328–331.
- Hemmingsen L, et al. (1999) Structure, chemical bonding, and nuclear quadrupole interactions of  $\beta\text{-Cd}(\text{OH})_2$ : Experiment and first principles calculations. *Inorg Chem* 38(12):2860–2867.
- Cairns RW, Ott E (1933) X-ray studies of the system nickel–oxygen–water. I. Nickelous oxide and hydroxide. *J Am Chem Soc* 55:527–533.
- Lutz HD, Möller M, Schmidt M (1994) Lattice vibration spectra. Part LXXXII. Brucite-type hydroxides  $\text{M}(\text{OH})_2$  (M = Ca, Mn, Co, Fe, Cd)–IR and Raman spectra, neutron diffraction of  $\text{Fe}(\text{OH})_2$ . *J Mol Struct* 328:121–132.
- Meade C, Jeanloz R (1990) Static compression of  $\text{Ca}(\text{OH})_2$  at room temperature: Observations of amorphization and equation of state measurements to 10.7 GPa. *Geophys Res Lett* 17:1157–1160.
- Parise JB, Leinenweber K, Weidner DJ, Tan K, Von Dreele RB (1994) Pressure-induced H bonding: Neutron diffraction study of brucite,  $\text{Mg}(\text{OH})_2$ , to 9.3 GPa. *Am Mineral* 79:193–196.
- Catti M, Ferraris G, Hull S, Pavese A (1995) Static compression and H disorder in brucite,  $\text{Mg}(\text{OH})_2$ , to 11 GPa: A powder neutron diffraction study. *Phys Chem Miner* 22:200–206.
- Kruger MB, Williams G, Jeanloz R (1989) Vibrational spectra of  $\text{Mg}(\text{OH})_2$  and  $\text{Ca}(\text{OH})_2$  under pressure. *J Chem Phys* 91:5910–5915.
- Duffy TS, Meade C, Fei Y, Mao HK, Hemley RJ (1995) High-pressure phase transition in brucite,  $\text{Mg}(\text{OH})_2$ . *Am Mineral* 80:222–230.
- Raugei S, Silvestrelli P, Parrinello M (1999) Pressure-induced frustration and disorder in  $\text{Mg}(\text{OH})_2$  and  $\text{Ca}(\text{OH})_2$ . *Phys Rev Lett* 83:2222–2225.
- Mookherjee M, Stixrude L (2006) High-pressure proton disorder in brucite. *Am Mineral* 91:127–134.
- Loveday JS, et al. (1996) The structure and structural pressure dependence of sodium deuteriooxide–V by neutron powder diffraction. *J Phys Condens Matter* 8:L597–L604.
- Hermann A, Ashcroft NW, Hoffmann R (2014) Lithium hydroxide,  $\text{LiOH}$ , at elevated densities. *J Chem Phys* 141(2):024505.
- Hermann A, Guthrie M, Nelmis RJ, Loveday JS (2015) Pressure-induced localisation of the hydrogen-bond network in  $\text{KOH-VI}$ . *J Chem Phys* 143(24):244706.
- Hermann A (2016) High-pressure phase transitions in rubidium and caesium hydroxides. *Phys Chem Chem Phys* 18(24):16527–16534.
- Oganov AR, Ono S (2004) Theoretical and experimental evidence for a post-perovskite phase of  $\text{MgSiO}_3$  in Earth's D" layer. *Nature* 430(6998):445–448.
- Tsuchiya J (2013) First principles prediction of a new high-pressure phase of dense hydrous magnesium silicates in the lower mantle. *Geophys Res Lett* 40:4570–4573.
- Nishi M, et al. (2014) Stability of hydrous silicate at high pressures and water transport to the deep lower mantle. *Nat Geosci* 7:224–227.
- Fei Y, Mao H-K (1993) Static compression of  $\text{Mg}(\text{OH})_2$  to 78 GPa at high temperature and constraints on the equation of state of fluid  $\text{H}_2\text{O}$ . *J Geophys Res Solid Earth* 98:11875–11884.
- Ma M, Liu W, Chen Z, Liu Z, Li B (2013) Compression and structure of brucite to 31 GPa from synchrotron X-ray diffraction and infrared spectroscopy studies. *Am Mineral* 98:33–40.
- Dziewonski AM, Anderson DL (1981) Preliminary reference Earth model. *Phys Earth Planet Inter* 25:297–356.
- Dion M, Rydberg H, Schröder E, Langreth DC, Lundqvist BI (2004) van der Waals density functional for general geometries. *Phys Rev Lett* 92(24):246401.
- Román-Pérez G, Soler JM (2009) Efficient implementation of a van der Waals density functional: Application to double-wall carbon nanotubes. *Phys Rev Lett* 103(9):096102.
- Klimeš J, Bowler DR, Michaelides A (2010) Chemical accuracy for the van der Waals density functional. *J Phys Condens Matter* 22(2):022201.
- Klimeš J, Bowler D, Michaelides A (2011) Van der Waals density functionals applied to solids. *Phys Rev B* 83:195131.
- Eberle MA, Grasset O, Sotin C (2002) A numerical study of the interaction between the mantle wedge, subducting slab, and overriding plate. *Phys Earth Planet Inter* 134:191–202.
- Bina CR, Navrotsky A (2000) Possible presence of high-pressure ice in cold subducting slabs. *Nature* 408(6814):844–847.
- Dubrovinskaya N, Dubrovinsky L (2003) Melting curve of water studied in externally heated diamond-anvil cell. *High Press Res* 23:307–311.
- Goncharov AF, et al. (2005) Dynamic ionization of water under extreme conditions. *Phys Rev Lett* 94(12):125508.
- Cerotti M, et al. (2016) Nuclear quantum effects in water and aqueous systems: Experiment, theory, and current challenges. *Chem Rev* 116(13):7529–7550.
- Jiang F, Speziale S, Duffy TS (2006) Single-crystal elasticity of brucite,  $\text{Mg}(\text{OH})_2$ , to 15 GPa by Brillouin scattering. *Am Mineral* 91:1893–1900.
- Bader RFW (1994) *Atoms in Molecules: A Quantum Theory* (Oxford Univ Press, Oxford).
- Libowitzky E (1999) *Hydrogen Bond Research*, eds Schuster P, Mikenda W (Springer, Vienna), pp 103–115.
- Hermansson K, Gajewski G, Mitev PD (2008) Pressure-induced OH frequency downshift in brucite: Frequency-distance and frequency-field correlations. *J Phys Conf Ser* 117:012018.
- Mitev PD, Gajewski G, Hermansson K (2009) Anharmonic OH vibrations in brucite: Small pressure-induced redshift in the range 0–22 GPa. *Am Mineral* 94:1687–1697.
- Tsuchiya J, Tsuchiya T, Tsuneyuki S, Yamanaka T (2002) First principles calculation of a high-pressure hydrous phase,  $\delta\text{-AlOOH}$ . *Geophys Res Lett* 29:1909.
- Tsuchiya J, Mookherjee M (2015) Crystal structure, equation of state, and elasticity of phase H ( $\text{MgSiO}_3\text{H}_2$ ) at Earth's lower mantle pressures. *Sci Rep* 5:15534.
- Hushur A, et al. (2011) Hydrogen bond symmetrization and equation of state of phase D. *J Geophys Res Solid Earth* 116:B06203.
- Goncharov AF, Struzhkin VV, Mao H, Hemley RJ (1999) Raman spectroscopy of dense  $\text{H}_2\text{O}$  and the transition to symmetric hydrogen bonds. *Phys Rev Lett* 83:1998–2001.
- Bronstein Y, Depondt P, Finocchii F, Saitta AM (2014) Quantum-driven phase transition in ice described via an efficient Langevin approach. *Phys Rev B* 89:214101.
- Tongamp W, Zhang Q, Saito F (2007) Preparation of meixnerite ( $\text{Mg-Al-OH}$ ) type layered double hydroxide by a mechanochemical route. *J Mater Sci* 42:9210–9215.
- Xue X, Kanzaki M (2007) High-pressure  $\delta\text{-Al}(\text{OH})_3$  and  $\delta\text{-AlOOH}$  phases and isostructural hydroxides/oxyhydroxides: New structural insights from high-resolution  $^1\text{H}$  and  $^{27}\text{Al}$  NMR. *J Phys Chem B* 111(46):13156–13166.
- Matsui M, et al. (2011) The crystal structure of  $\delta\text{-Al}(\text{OH})_3$ : Neutron diffraction measurements and ab initio calculations. *Am Mineral* 96:854–859.
- Pamato MG, et al. (2014) Lower-mantle water reservoir implied by the extreme stability of a hydrous aluminosilicate. *Nat Geosci* 8:75–79.
- Asahara Y, Hirose K, Ohishi Y, Hirao N, Murakami M (2010) Thermoelastic properties of ice VII and its high-pressure polymorphs: Implications for dynamics of cold slab subduction in the lower mantle. *Earth Planet Sci Lett* 299:474–482.
- Lawrence JF, Wyssession ME (2006) *Earth's Deep Water Cycle*, eds Jacobsen SD, Van der Lee S (American Geophysical Union, Washington, DC), pp 251–261.
- Ghosh S, Schmidt MW (2014) Melting of phase D in the lower mantle and implications for recycling and storage of  $\text{H}_2\text{O}$  in the deep mantle. *Geochim Cosmochim Acta* 145:72–88.
- Kresse G, Furthmüller J (1996) Efficient iterative schemes for ab initio total-energy calculations using a plane-wave basis set. *Phys Rev B Condens Matter* 54(16):11169–11186.
- Blöchl PE (1994) Projector augmented-wave method. *Phys Rev B Condens Matter* 50(24):17953–17979.
- Kresse G, Joubert D (1999) From ultrasoft pseudopotentials to the projector augmented-wave method. *Phys Rev B* 59:1758–1775.
- Perdew JP, Burke K, Ernzerhof M (1996) Generalized gradient approximation made simple. *Phys Rev Lett* 77(18):3865–3868.
- Lonie DC, Zurek E (2011) XtalOpt: An open-source evolutionary algorithm for crystal structure prediction. *Comput Phys Commun* 182:372–387.
- Wang Y, Lv J, Zhu L, Ma Y (2012) CALYPSO: A method for crystal structure prediction. *Comput Phys Commun* 183:2063–2070.
- Alfé D (2009) PHON: A program to calculate phonons using the small displacement method. *Comput Phys Commun* 180:2622–2633.
- Karki BB, Stixrude L, Wentzcovitch RM (2001) High-pressure elastic properties of major materials of earth's mantle from first principles. *Rev Geophys* 39:507–534.
- Nye JF (1957) *Physical Properties Of Crystals: Their Representation by Tensors and Matrices* (Oxford Univ Press, Oxford).
- Mainprice D (1990) A FORTRAN program to calculate seismic anisotropy from the lattice preferred orientation of minerals. *Comput Geosci* 16:385–393.
- Zha C-S, Mao H, Hemley RJ (2000) Elasticity of  $\text{MgO}$  and a primary pressure scale to 55 GPa. *Proc Natl Acad Sci USA* 97(25):13494–13499.